Inorganic Chemistry

ARTICLE

pubs.acs.org/IC

Synthesis, Magnetic Properties, and Magnetic Structure of a Natrochalcite Structural Variant, $KM^{II}{}_2D_3O_2(MoO_4)_2$ (M = Mn, Fe, or Co)

Wassim Maalej,[†,‡] Serge Vilminot,[*,†] Gilles André,[§] Françoise Damay,[§] Zakaria Elaoud,[‡] Tahar Mhiri,[‡] and Mohamedally Kurmoo[*,||]

[†]Département de Chimie des Matériaux Inorganiques, IPCMS, UMR 7504 (CNRS-UDS), 23 rue du Loess, BP 43, 67034 Strasbourg Cedex 02, France

[‡] Laboratoire de l'Etat Solide, Faculté des Sciences, Université Sfax, route de Soukra km 3.5, 3018 Sfax, Tunisia

[§]Laboratoire Léon Brillouin, CEA-CNRS, CEA Saclay, 91191 Gif-sur-Yvette, France

[||]Laboratoire DECOMET, CNRS-UMR 7177, Université de Strasbourg, CS 90032, 4 rue Blaise Pascal, 67081 Strasbourg Cedex, France

Supporting Information

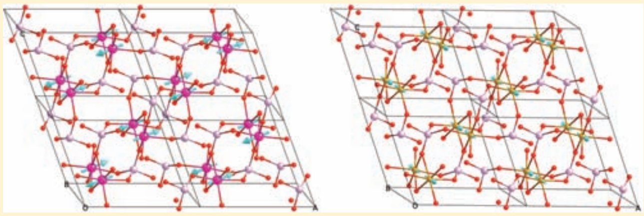

ABSTRACT: We report the syntheses, crystal structures, and magnetic properties of $KMn_2(H_3O_2)(MoO_4)_2$ (**MnH**), $KMn_2(D_3O_2)(MoO_4)_2$ (**MnD**), $KFe_2(H_3O_2)(MoO_4)_2$ (**FeH**), $KFe_2(D_3O_2)(MoO_4)_2$ (**FeD**), $KCo_2(H_3O_2)(MoO_4)_2$ (**CoH**), and $KCo_2(D_3O_2)(MoO_4)_2$ (**CoD**), and the magnetic structures of **MnD** and **FeD**. They belong to the structural variant (space group $I2/m$) of the mineral natrochalcite $NaCu_2(H_3O_2)(SO_4)_2$ (space group $C2/m$) where the diagonal within the *ac*-plane of the latter become one axis of the former. The structure of **MnD**, obtained from Rietveld refinement of a high-resolution neutron pattern taken at 300 K, consists of chains of edge-sharing octahedra bridged by MoO_4 and D_3O_2 to form layers, which are connected to K through the oxygen atoms to form the three-dimensional (3D)-network. The X-ray powder diffraction patterns of the other two compounds were found to belong to the same space group with similar parameters. The magnetic susceptibilities of **MnH** and **FeH** exhibit long-range ordering of the moments at a Néel temperature of 8 and 11 K, respectively, which are accompanied by additional strong Bragg reflections in the neutron diffraction in the ordered state, consistent with antiferromagnetism. Analyses of the neutron data for **MnD** and **FeD** reveal the presence of both long- and short-range orderings and commensurate magnetic structures with a propagation vector of $({}^1/_2, 0, {}^1/_2)$. The moments are antiferromagnetically ordered within the chains with alternation between chains to generate four nonequivalent nuclear unit cells. For **MnD** the moments are perpendicular to the chain axis (*b*-axis) while for **FeD** they are parallel to the *b*-axis. The overall total is a fully compensated magnetic structure with zero moment in each case. Surprisingly, for $KCo_2(D_3O_2)(MoO_4)_2$ neither additional peaks nor increase of the nuclear peaks' intensities were observed in the neutron diffraction patterns below the magnetic anomaly at 12 K which was identified to originate from a small quantity of a ferromagnetic compound, $Co_2(OH)_2MoO_4$.

INTRODUCTION

The mineral Natrochalcite, $NaCu_2(H_3O_2)(SO_4)_2$,[1] may be regarded as second to the spinels (MM'_2O_4) where every component in the content can be chemically replaced, for example, Na by K, Ag, Tl, Rb, and NH_4; Cu by Mn, Fe, Co, and Ni; H by D; and SO_4 by SeO_4 and MoO_4, as well as making solid solutions.[2−5] From this whole gamut of materials, one can study the effect of the size of the components on the crystal engineered. Much is known about the structures from both single crystal and powder X-ray and neutron diffractions.[2−4] The early studies concentrated on the crystal systems and in particular, on the geometry of the $H_3O_2^-$ ion that bridges the metals. The structures consist of chains of edge-sharing octahedra that are bridged by the H_3O_2 and the tetrahedral anions into sheets. The sheets are then connected by the alkali metals to form the three-dimensional (3D)-network.

Our interest in this series followed our work on Antlerite,[6] $Cu_3(OH)_4(ZO_4)$ (Z = S or Se) and Lindgrenite, $Cu_3(OH)_2(MoO_4)_2$,[7] where we observed antiferromagnetism with a collinear magnetic structure for $Cu_3(OH)_4(SO_4)$ but a cycloidal one for $Cu_3(OH)_4(SeO_4)$ while a ferrimagnetic long-range order at 13 K with a collinear magnetic structure for $Cu_3(OH)_2(MoO_4)_2$. For the latter the neutron diffraction study reveals a magnetic structure where the edge-shared copper atoms have their moments parallel and they are antiparallel to those of the corner-shared copper atoms within the diamond chains. The equivalent cobalt and nickel compounds are not known, and the syntheses using these metals resulted in the formation of natrochalcite analogues, $NaM_2(H_3O_2)(MoO_4)_2$.[8] Interestingly, the magnetic structures ($k = 0, 0, 0$) in the two cases consist of their moments

Received: September 23, 2010
Published: March 23, 2011

within each edge-sharing metal chain being ferromagnetically aligned but the directions depend on the metal, and the ground states are antiferromagnetic because of antiferromagnetic coupling between the chains. Because of the variations in magnetic structures, we decided to explore the crystal chemistry, magnetism, and magnetic structures of other members of the natrochalcite family and in particular, with other transition metals and alkali metals. Here, we present the results of three of them, $KM_2(H_3O_2)(MoO_4)_2$, M = Mn, Fe, or Co, where we opted for a large alkali metal that is expected to separate the layers further apart. The results are quite surprising. In contrast with $NaM_2(D_3O_2)(MoO_4)_2$, they adopt a different space group, and the long-range antiferromagnetic orderings for $KMn_2(D_3O_2)(MoO_4)_2$ and $KFe_2(D_3O_2)(MoO_4)_2$ involve antiparallel moments within each chains and are characterized by a complex magnetic structure ($k = {}^1/_2, 0, {}^1/_2$) involving a magnetic unit cell four times the nuclear cell. On the other hand for $KCo_2(D_3O_2)(MoO_4)_2$ the neutron diffraction experiments indicate no long-range magnetic ordering above 1.6 K.

■ EXPERIMENTAL SECTION

Synthesis. $MnCl_2 \cdot 4H_2O$ (1.979 g, 10 mmol) and molybdic acid H_2MoO_4 (2.429 g, 15 mmol) were dissolved in 35 mL of boiling distilled water to give a yellow solution. KOH (1.98 g of 85 wt %, 30 mmol) in 5 mL of boiled distilled water was then poured into the yellow solution giving rise to an immediate precipitation of a pale beige powder. The suspension was then introduced into a 125 mL autoclave, which was sealed and heated under autogenous pressure at 150 °C for 48 h. A beige powder (**MnH**) was retrieved from the mother liquor, washed with water, ethanol, and acetone and dried in air at 50 °C. The yield was 88%. For neutron scattering measurements, D_2O was used in the place of H_2O, and the synthesis results, all other conditions being equal, in a beige powder (**MnD**). Analyses, Calcd (found) % for **MnH**: K 7.76 (7.87); Mo 38.08 (38.95); M_n 21.81 (23.60).

$KFe_2(H_3O_2)(MoO_4)_2$ was prepared by the hydrothermal treatment of a mixture of iron(II) sulfate heptahydrate $FeSO_4 \cdot 7H_2O$ (1.85 g, 6.65 mmol in 20 mL H_2O) and potassium molybdate K_2MoO_4 (4.76 g, 20 mmol in 20 mL H_2O) at 210 °C for 24 h. The water was boiled and degassed before use to lower the oxidation of the iron(II). After cooling to room temperature the products, shiny red crystals and some dark particles, were washed with distilled water, ethanol, and acetone followed by drying in air. Crystals of $KFe_2(H_3O_2)(MoO_4)_2$ were contaminated with some black particles (see Supporting Information, Figure S1) of α-Fe_2O_3 (JCPDS-89-599) and Fe_3O_4 (JCPDS-88-866). $KFe_2(D_3O_2)(MoO_4)_2$ was obtained using the same procedure but from heavy water. Analyses, Calcd (found) % for **FeH**: K 7.69 (6.45); Mo 37.72 (36.06); Fe 21.96 (23.84).

The corresponding cobalt samples (**CoH** and **CoD**) together with a small quantity of $Co_2(OH)_2MoO_4$ (see Supporting Information) were obtained as light purple powders from an aqueous mixture of $Co(NO_3)_2 \cdot 6H_2O$ or $CoCl_2 \cdot 6H_2O/H_2MoO_4$/KOH in the relative molar proportions 1/1.5/3 at 150 °C for 20−24 h. Yields were about 85%. **CoD** was prepared in D_2O for neutron diffraction measurements. If the temperature is 210 or 230 °C, with the same proportions of reagents, $Co_2(OH)_2MoO_4$ is obtained. For intermediate temperatures, a mixture of both compounds is detected. Starting from a 1/1/1 ratio at 200−230 °C, $CoMoO_4 \cdot 0.5H_2O$ is obtained while starting with 1/1.5/1.5 ratio the anhydrous $CoMoO_4$ is the product. Analyses, Calcd (found) % for **CoH**: K 7.64 (7.16); Mo 37.49 (36.95); Co 23.03 (22.91).

Characterizations. Infrared spectra were recorded using a Digilab Excalibur Series FTIR spectrometer by transmission through KBr pellets containing about 1% of the compounds. Powder X-ray diffraction (XRD) patterns were recorded using a D8 Bruker diffractometer (Cu Kα_1, 1.5406 Å), equipped with a front monochromator. EDX analyses for the heavy metals were made using a Kevex unit on JEOL 6700 F scanning electronic microscope (SEM). Magnetic susceptibility measurements were performed in the range 2−300 K and ±50 kOe by means of a Quantum Design MPMS-XL SQUID magnetometer.

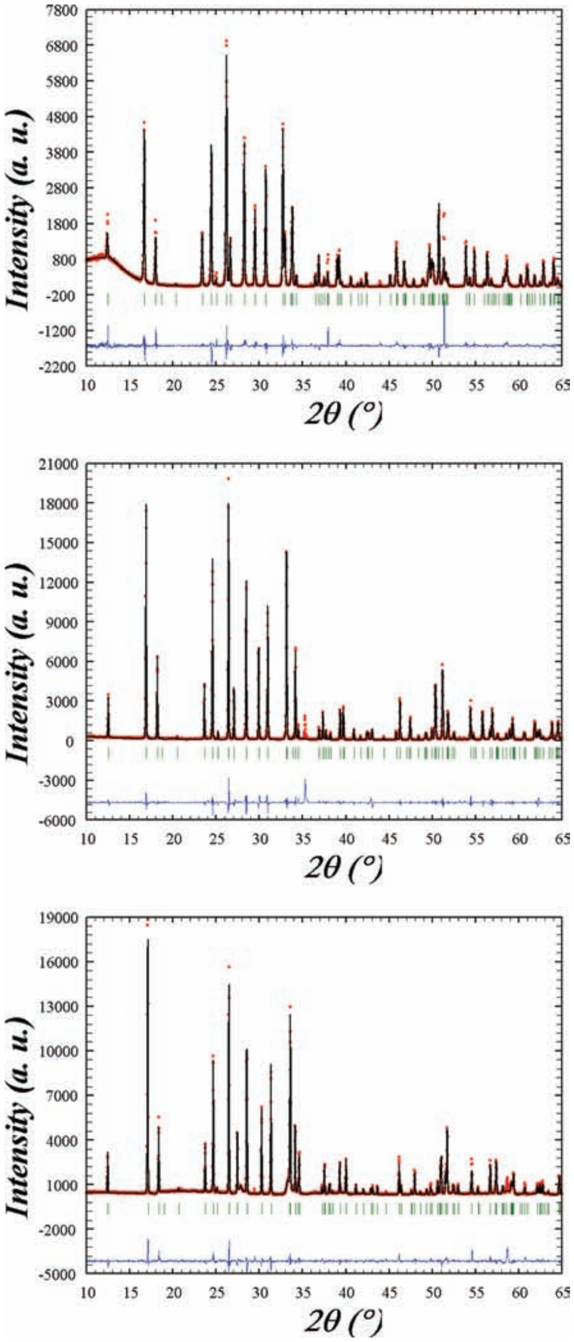

Figure 1. Observed (red circles) and calculated (black line) pattern matching profiles of the X-ray powder diffraction patterns of **MnD** (top), **FeH** (middle), and **CoH** (bottom) obtained on D8 Bruker diffractometer (λ = 1.5406 Å) at 300 K with position of the Bragg reflections (short green vertical lines) and difference between observed and calculated profiles (blue lines).

The neutron diffraction experiments were performed at the Laboratoire Léon Brillouin (CEA Saclay) using the multidetector (800 cells) G4.1 (λ = 2.4226 Å) diffractometer for the determination of the magnetic structure and its thermal evolution in the low temperature region for all three compounds, **MnD**, **FeD**, and **CoD**. The high-resolution 3T2 (λ = 1.2250 Å) powder diffractometer was employed for data collection

Table 1. Summary of the Refinements of Powder Diffraction Data

	MnD[a]	MnD[b]	FeD[c]	CoH[a]
method	X-ray	neutron	neutron	X-ray
temperature (K)	300 K	300 K	15 K	300 K
a (Å)	9.4636(1)	9.4649(5)	9.3636(4)	9.3655(1)
b (Å)	6.6862(1)	6.6868(3)	6.5597(3)	6.48793(9)
c (Å)	7.8969(1)	7.8983(4)	7.8264(4)	7.8596(1)
β (deg)	112.9279(7)	112.935(2)	112.521(3)	113.5496(5)
V (Å^3)	460.20(1)	460.37(4)	443.90(1)	437.80(1)
Z	2	2	2	2
space group	$I2/m$	$I2/m$	$I2/m$	$I2/m$
D_{calc} (g cm^{-3})	3.657	3.656	3.805	3.883
radiation λ (Å)	1.5406	1.2250	2.4226	1.5406
2θ range (deg)/step (deg)	10−67/0.02	10−120.95/0.05	11−91/0.1	10−67/0.02
no. of reflections	104	754	58	101
no. of parameters	31	39	21	31
R_p	12.3	5.89(S)/6.20(NS) [d]	11.3	14.6
R_{wp}	16.1	5.88(S)/6.23(NS)	11.5	15.7
R_B	5.78	2.51(S)/2.78(NS)	2.01	5.37
R_F	3.93	1.78(S)/1.91(NS)	1.81	5.45
GoF	4.53	2.15(S)/2.42 (NS)	23.8	5.85

[a] XRD data of D8 Bruker diffractometer. [b] Neutron diffraction data of 3T2 diffractometer. [c] Neutron diffraction data of G4.1 diffractometer. [d] S = model with split hydrogen positions, NS = model with centrally placed hydrogen position.

Table 2. Fractional Atomic Coordinates for MnD Obtained from Powder Neutron Diffraction Data on the 3T2 Diffractometer and from Powder XRD Data at 300 K (in italics)[a]

atom	x/a	y/b	z/c	B (Å^2)	occupancy
Mo	0.41653(18) *0.4168(3)*	0.5	0.70379(22) *0.7017(3)*	0.94(2) *3.01(8)*	0.5
Mn	0.75	0.75	0.75	1.31(5) *3.7(1)*	0.5
K	0.0	0.5	0.5	1.37(7) *3.4(2)*	0.25
OD	0.8508(2) *0.8528(12)*	0.5	0.9341(3) *0.9342(17)*	1.33(3) *4.8(4)*	0.5
O1	0.2825(2) *0.2842(15)*	0.5	0.8036(3) *0.8032(18)*	1.72(4) *5.9(5)*	0.5
O2	0.96590(14) *0.9669(11)*	0.78454(18) *0.7910(11)*	0.72562(17) *0.7127(12)*	1.35(2) *3.9(3)*	1.0
O3	0.3139(2) *0.3161(15)*	0.5	0.4553(3) *0.4785(18)*	1.35(3) *4.6(4)*	0.5
H1	0.1821(3)	0.5	−0.0360(3)	2.31(6)	0.056(1)
D1	0.1821(3)	0.5	−0.0360(3)	2.31(6)	0.444(1)
H2	0.0262(8)	0.5	0.0031(11)	2.54(13)	0.033(1)
D2	0.0262(8)	0.5	0.0031(11)	2.54(13)	0.217(1)

[a] D/(D+H) = 0.88.

of **MnD** at room temperature used for the refinement of the nuclear structure. Several diffraction patterns in the 2θ range 10−89.9° were recorded on G4.1 at fixed temperatures from above the magnetic anomalies observed in the susceptibility and 1.6 K. The powder samples were set in cylindrical vanadium cans and held in a liquid helium cryostat. Nuclear and magnetic structures were refined using the FULLPROF program.[9] The nuclear scattering lengths ($b_K = 0.3670 \times 10^{-12}$ cm, $b_{Mn} = -0.3730 \times 10^{-12}$ cm, $b_{Co} = 0.2490 \times 10^{-12}$ cm, $b_{Fe} = 0.9450 \times 10^{-12}$ cm, $b_{Mo} = 0.6715 \times 10^{-12}$ cm, $b_O = 0.5803 \times 10^{-12}$ cm, $b_H = -0.3739 \times 10^{-12}$ cm, and $b_D = 0.6671 \times 10^{-12}$ cm) and magnetic form factors for manganese and iron were those included in this program.

■ RESULTS AND DISCUSSION

Synthesis. The synthesis of the hydrogenated samples have been performed several times under different conditions varying the concentration of reagents, temperature, time, and filling factor of the autoclaves. While for manganese and cobalt the products were fine powders, for iron transparent red small crystals were obtained. In the case of the cobalt compound, three more phases, $Co^{II}_2(OH)_2MoO_4$, $Co^{II}(MoO_4)(H_2O)_{0.5}$, and $Co^{II}(MoO_4)$ were identified under certain conditions. Following characterizations the conditions were optimized for obtaining single phase and also for higher crystallinity by observing the XRD line width. The final optimized conditions were then used for the preparations of the deuterated samples. Preparations of the manganese compounds performed at higher temperatures to promote the formation of single crystals always yield the formation of a black powder resulting from the oxidation of Mn(II). This is less so for the cobalt compounds. Increasing the alkalinity of the starting mixture always produced black oxides in both cases. For iron, the products are always accompanied with a sparing amount of dark oxides under all conditions. The failure to obtain large

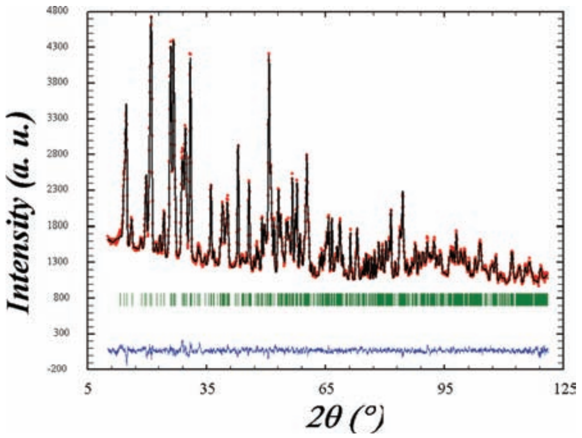

Figure 2. Observed (red circles) and calculated (black line) profiles of the powder neutron diffraction pattern of **Mn-D** obtained on the 3T2 diffractometer (λ = 1.2250 Å) at 300 K with position of the Bragg reflections (short vertical lines) and difference between observed and calculated profiles (blue line).

crystals as in the case of the sodium analogue of cobalt may be due to the matching of the cationic sizes, K and Co.

X-ray Diffraction. The powder XRD patterns appear to be significantly different from the ones obtained for typical natrochalcite $NaM_2(H_3O_2)(MoO_4)_2$, M = Co, Ni.[2,3,8] Using the indexing DICVOL program,[10] a unit cell of **MnD** with the following parameters a = 9.4631(8) Å, b = 6.6845(5) Å, c = 7.8956(7) Å, β = 112.939(6)°, V = 459.95 Å^3 was found with high figures of merit, M(20) = 51.6 and F(20) = 75.2 (Figure 1). These parameters allow one to index all the lines of the X-ray powder diffractogram. Consideration of the systematic absences suggested the $I2/m$ space-group. Coincidently, the unit cell parameters appear very close to the ones exhibited by the natrochalcite samples, a = 9.3557(9) Å, b = 6.3269(6) Å, c = 7.6248(7) Å, β = 115.784(2)°, V = 406.40(7) Å^3 for $NaCo_2(H_3O_2)(MoO_4)_2$.[8] However, the main difference concerns the space group, which is changed from $C2/m$ for the known natrochalcite samples to $I2/m$. However, these two space groups only differ by the choice of the orientation of the unit cell. The X-ray powder patterns for **CoH**, **CoD**, **FeH**, and **FeD** are similar to those of **MnH** and **MnD**, suggesting that these compounds are isostructural. However, the diffraction lines of **CoD** are broader than those of **MnH** and **CoH**. Therefore the refinement of the structure was performed on data of **CoH**. Similar unit cell parameters were obtained for **FeH** and **CoH** (Table 1), but there were some extra lines belonging to α-Fe_2O_3 (JCPDS-89-599) and Fe_3O_4 (JCPDS-88-866) for the former and to $Co^{II}{}_2(OH)_2MoO_4$ for the latter. The unit cell parameters decrease in the order **MnD** > **FeH** > **CoH** in agreement with the ionic radii.[11]

Thermal Analysis. Thermogravimetric analysis (TGA) of **MnH** recorded under air (Supporting Information, Figure S2) reveals a weight loss between 255 and 380 °C accompanied by an endotherm peaking at 278 °C. It has been attributed to the departure of $1.5H_2O$ from the H_3O_2 group, calcd 5.36%, obs. 4.94%. At higher temperatures weight increases are observed which are associated with the oxidation of manganese. As the calculated and observed weight losses differ by about 8%, a TGA experiment has been performed under argon to avoid the oxidation of manganese during the first step below 380 °C. In the corresponding trace, the agreement is much better, calcd 5.36%, obs. 5.46%. The thermal analysis is a first result concerning the chemical formula.

Table 3. Distances (Å) and Angles (deg) for MnD Obtained from Data Recorded at 300 K on the 3T2 Diffractometer

atoms	distance	atoms	angle
	Mn Environment		
Mn−OD	2.1764(11) ×2	OD−Mn−OD	180.00(9)
Mn−O2	2.1384(15) ×2	OD−Mn−O2	87.58(10) ×2
Mn−O3	2.2416(13) ×2	OD−Mn−O2	92.42(10) ×2
<Mn−O>	2.185	OD−Mn−O3	80.49(10) ×2
		OD−Mn−O3	99.51(5) ×2
		O2−Mn−O2	180.00(12)
		O2−Mn−O3	90.77(9) ×2
		O2−Mn−O3	89.23(11) ×2
		O3−Mn−O3	180.00(10)
	Mo Environment		
Mo−O1	1.735(3)	O1−Mo−O2	109.73(18) ×2
Mo−O2	1.7724(15) ×2	O1−Mo−O3	108.2(2)
Mo−O3	1.820(2)	O2−Mo−O2	108.76(11)
<Mo−O>	1.775	O2−Mo−O3	110.19(13) ×2
	K Environment		
atom	distance	atom	distance
K−O1	2.8112(18) ×2	O1−K−O1	180.00(11)
K−O2	2.7108(14) ×4	O1−K−O2	75.91(7) ×4
<K−O>	2.744	O1−K−O2	104.09(8) ×4
		O2−K−O2	90.84(8) ×2
		O2−K−O2	180.00(9) ×2
		O2−K−O2	89.16(6) ×2
	Deuterium Bonding		
atoms	distance	atoms	angle
D1−OD	0.969(4)	OD−D1···O1	169.0(4)
D1···O1	1.857(4)	D1−OD−D2	104.9(9)
D2−OD	1.073(7)	D1−OD−D2′	111.0(8)
D2−OD′	1.533(7)	OD−D2−OD	173.9(5)
D1−D2	1.620(9)		
D1−D2′	2.086(9)		
D2−D2′	0.479(11)		

The DT-TGA of **FeH** in air (Supporting Information, Figure S3) exhibits a mass loss of about 2% between 207 and 379 °C which is lower than those of other metals studied so far. The mass loss is accounted by the concomitant departure of H_3O_2 and the oxidation of the Fe(II) to Fe(III) according to the equation: $KFe_2H_3O_2(MoO_4)_2 \rightarrow KFe(MoO_4)_2 + {}^1/{}_2Fe_2O_3$ $\Delta P/P = 2.2\%$. The products of this reaction were confirmed by an XRD measurement of a sample heated to 800 °C.

For **CoH** a similar behavior to **MnH** (Supporting Information, Figure S4) is observed where the weight loss takes place at higher temperatures between 345 and 465 °C and the endotherm having a maximum at 373 °C. It has been attributed to the departure of $1.5H_2O$ where the agreement is also better under Ar atmosphere which prevents the oxidation of Co(II), calcd 5.27%, obs. 4.76% (air), obs. 5.23% (Ar).

SEM Observations and EDX Analyses. Scanning electron microscopy (SEM) images (Supporting Information, Figure S5)

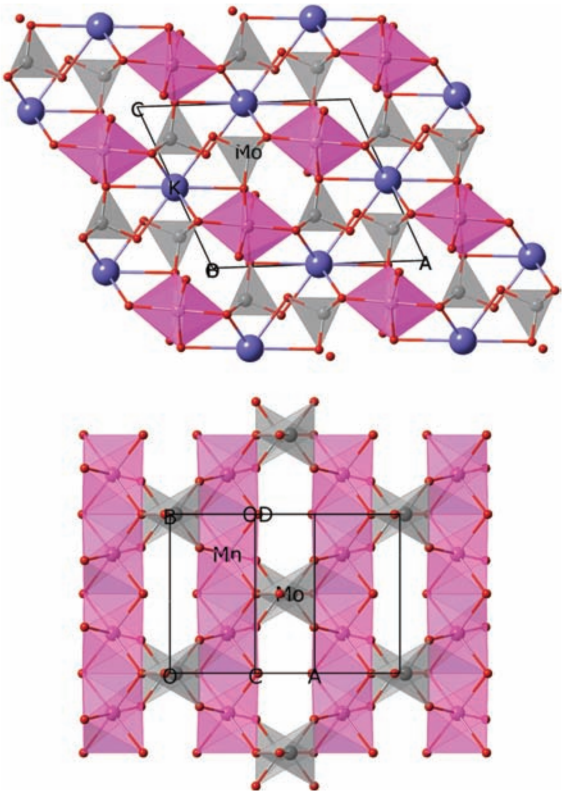

Figure 3. Projection of the structure of **MnD** along the *b*-axis (top) and perpendicular to it (bottom) showing the connections of the edge-sharing chains by the MoO_4 and K.

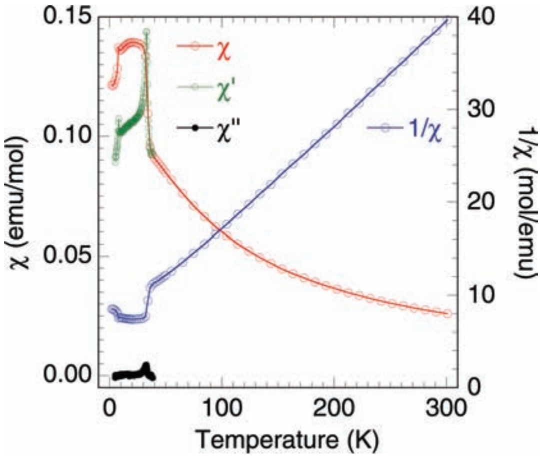

Figure 4. Temperature dependence of the dc-magnetic susceptibility (red), its inverse (blue) in an applied field of 100 Oe, and the ac-susceptibilities (real green and imaginary black) for **MnH** in a field of 3.5 Oe oscillating at 20 Hz.

reveal the presence of small crystallites with dimensions varying between 70 and 330 nm having a diamond habit for the best developed **MnD** ones, while they are of spheroïdal habit for the smaller **CoD**. Energy dispersive X-ray (EDX) analyses were performed on pellets obtained by compression of the powder. The mean values of 5 measurements are Mo 41.1 atom % (calc 40.0 atom %), K 18.5 atom % (calcd 20 atom %), Mn 40.3 atom % (calc 40.0 atom %) and Mo 41.8 atom % (calc 40.0 atom %), K 18.5 atom % (calc 20 atom %), Co 39.6 atom % (calc 40.0 atom %) and confirm the formulation of **MnD** and **CoD**.

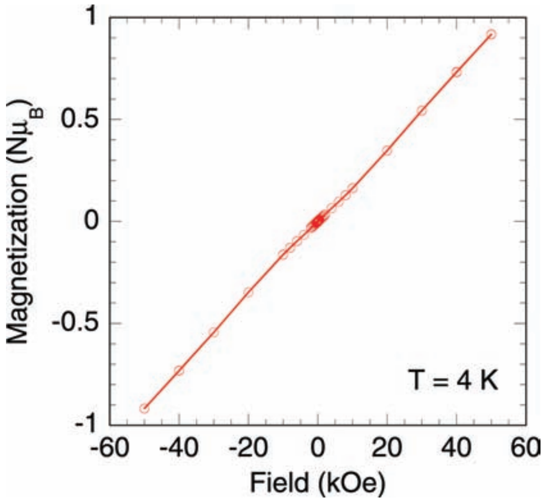

Figure 5. Isothermal magnetization for **MnH** at 4 K.

Infrared Spectroscopy. Comparison of the infrared spectra of **MnH** and **MnD** allows one to distinguish between the vibrational bands related to O−H(D) or MoO_4 (Supporting Information, Figure S6); the first ones being shifted by a factor of around 0.75 from **MnH** to **MnD**. The O−H(D) valence vibrations appear as two broad bands at 3435 and 3215 cm^{-1} (2556 and 2390 cm^{-1}) and their shapes suggest that the OH(D) groups are involved in hydrogen bonds as confirmed by the structural determinations. Two other families of bands of **MnH** are also shifted in **MnD**. The bands of MoO_4 obscure several of those of **MnH** and **MnD**. However, the following correspondences can be drawn: for $(H_3O_2)^-$ bands of **MnH** at 1590 and 1092, 807 (overlap with MoO_4 band) and 723 cm^{-1} to $(D_3O_2)^-$ bands of **MnD** at 1173, 810 (overlap with MoO_4 band), 601 and 534 cm^{-1}. These bands can be related to O−H(D)−O bending vibrations of the $H_3O_2^-$ anion. Finally, the MoO_4 vibration modes appear as four strong bands at 923 (926) cm^{-1} attributed to ν_1 that becomes IR active because of the deformation of the tetrahedron and at 879 (879), 850 (853), and 786 (785) cm^{-1} attributed to ν_3.[12,13] The band at around 405 cm^{-1} could be related to Mn−OH(D) vibration. Similar spectra were observed for the iron and cobalt samples (Supporting Information, Figures S7 and S8) and the results are given in Supporting Information, Table S1.

Determination of the Nuclear Structures. Refinement of the unit cell and profile parameters of the powder patterns allowed the calculation of the diffraction intensities of the *hkl* planes, which were then used for refinement of the structures by means of the direct methods of the SHELX program.[14] First solution is proposed involving the heavy atoms K, Mn, Fe or Co and Mo. After refinement of their positions, a difference Fourier reveals the positions of the oxygen atoms. At this stage, the structural model has been refined from diffraction data using the Rietveld method of the Fullprof program.[9] Table 1 gives a summary of the refinements, Table 2 and Supporting Information, Tables S2 and S3 list the atomic coordinates, and Figure 2 shows the corresponding observed and calculated patterns.

The quality of the refinements depends strongly on the resolution of the diffractometer used and the wavelength of excitation. The best refinement was observed for the high-resolution 3T2 neutron data measured with 1.2250 Å. Although

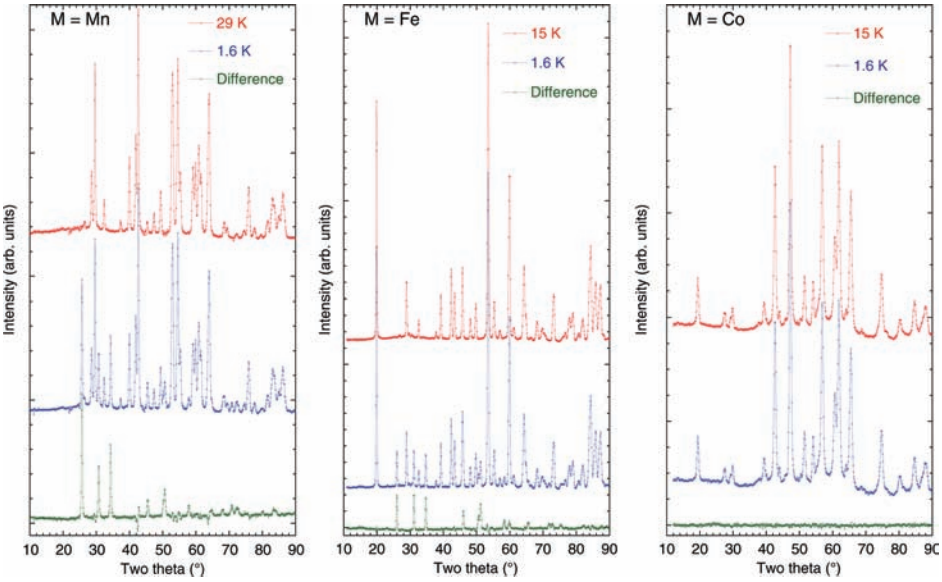

Figure 6. Neutron diffraction patterns below T_N (blue), above T_N (red), and the difference between the two (green) for **MnD** (left), **FeD** (center), and **CoD** (right).

Table 4. Positions and Indexing of the Observed Magnetic Bragg Peaks

K−Mn−MoD		K−Fe−MoD	
2*θ* (deg)	(*h k l*)	2*θ* (deg)	(*h k l*)
25.68	$(010)^+$ $(010)^-$	25.96	$(010)^+$ $(010)^-$
30.75	$(-111)^-$ $(210)^-$	31.11	$(-111)^-$ $(210)^-$
34.31	$(-111)^+$	34.69	$(-111)^+$
45.36	$(020)^+$ $(020)^-$	46.05	$(020)^+$ $(020)^-$
50.63	$(-302)^+$ $(-212)^+$	50.56	$(111)^+$
57.86	$(012)^+$	51.24	$(210)^+$ $(-212)^+$
70.88	$(-313)^+$	58.38	$(012)^+$
72.36	$(-113)^+$	71.87	$(-131)^-$ $(230)^-$

the X-ray data on the Bruker diffractometer show fairly fine lines, their lineshapes and intensity distributions resulted in poor refinement results. Thus, the structure determination of **MnD** is the most accurate and this is the one we discuss further.

The data recorded on the high-resolution 3T2 diffractometer permit the refinement of the structure of **MnD** including the fractional occupancies of the D and H atoms (Figure 2). Starting from the atomic positions of the heavy elements obtained from X-ray data analyses, two models have been tried; one is where the deuterium D2 bridging the oxygen atoms of the D_3O_2 is centrally placed (here labeled as "nonsplit") and the other is where it occupies two noncentrally placed equivalent positions (model "split").[4] The refinement using a split position for **MnD** yields a small decrease of the R factors compared to the case where D2 is located on the center of symmetry $(0, {}^1/_2, 0)$. Moreover, the isotropic temperature factor value (2.54) for the split position is much closer to the corresponding value for the D1 atom (2.31) than for the nonsplit one (4.02). Therefore, the split model appears more plausible. Table 1 gives a summary of the refinements, Table 2 the final atomic positions, Table 3 selected bond lengths and angles, and Figure 2 the observed and calculated profiles of the neutron powder pattern.

Table 5. Basis Functions of the Irreducible Representations Γ_1 and Γ_3[a]

	Γ_1			Γ_3		
	M_x	M_y	M_z	M_x	M_y	M_z
M11 0.125, 0.25, 0.125	+	+	+	+	+	+
M12 0.125, 0.75, 0.125	−	+	−	+	−	+
M13 0.375, 0.25, 0.375	−	+	−	+	−	+
M14 0.375, 0.75, 0.375	+	+	+	+	+	+

[a] Only for M1n atoms. The other ones are deduced with the same sequence for M4n (+ − − +) and opposite one for M2n and M3n (− + + −).

Description of the Structure. The structure of **MnD** consists of chains of edge-sharing MnO_6 octahedra running along the *b* axis (Figure 3). MoO_4 tetrahedra, polyhedra around the potassium atom, and $D_3O_2^-$ ions connect the chains and ensure the cohesion of the structure. The structure adopts the natrochalcite type with a rotation of the cell around the *b* axis as expected from the change of the space group from *C*2/*m* to *I*2/*m* (Supporting Information, Figure S9). The chains of MnO_6 are bridged by both MoO_4 and $D_3O_2^-$ to form sheets parallel to the plane containing the *b* axis and the diagonal of *a* and *c* axes. For the *C*2/*m* natrochalcite, these sheets are parallel to the *ab* plane. The MnO_6 octahedra are distorted with Mn−O distances varying from 2.134(2) to 2.244(2) Å, mean value 2.186 Å, that is, a distortion of (2.244 − 2.134)/2.186 of 5%. For $NaCo_2(D_3O_2)(MoO_4)_2$ refined from data also collected at 300 K on the 3T2 diffractometer,[8] the CoO_6 distortion was significantly lower, around 1.4%. MoO_4 tetrahedra with Mo−O distances between 1.729(5) and 1.814(4) Å, mean value 1.775 Å are also distorted (4.8%), a value smaller than the one observed for the Co compound. Concerning the environment of the potassium ion, if one restricts the bond lengths to the sum of the ionic radii, a 6-fold environment is observed, the resulting octahedron being strongly distorted with O−K−O angles varying between 73 and 104° instead of 90°. The Mn−Mn distances within the chains are 3.343 Å with O−Mn−O bridge angles of 96° and

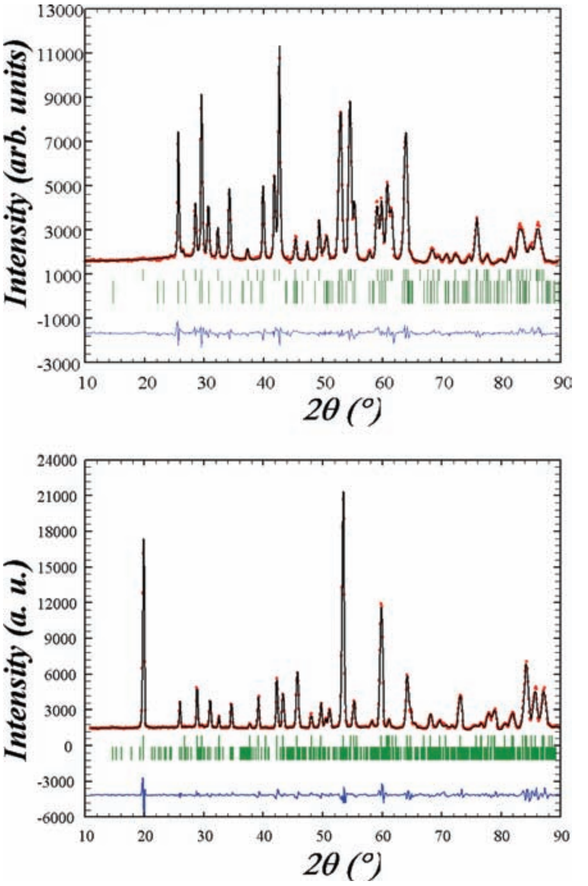

Figure 7. Observed (red circles) and calculated (black line) profiles of the neutron powder diffraction patterns of **MnD** (top) and **FeD** (bottom) obtained on the G4.1 diffractometer (λ = 2.4226 Å) at 1.6 K with position of the Bragg reflections (short vertical lines) and difference between observed and calculated profiles (blue line).

100° and provide the primary magnetic exchange pathway. The other connections (MoO_4, $D_3O_2^-$, and KO_6) are the secondary magnetic pathways. The oxygen atoms are of μ_2 (O1 and OD) or μ_3 (O2 and O3) types for bonds that do not involve hydrogen bonding. The refinement leads us to conclude to a splitting of the D2 position. Therefore, the hydrogen bond involving OD−D2···OD is not symmetrical as it would be for the D2 atom on the center of symmetry. However, we can define it as a strong oxygen bond since the OD···OD distance is much shorter than the sum of the ionic radii, 2.602 and 3.04 Å, respectively. The shortening due to hydrogen bond is 0.44 Å and slightly smaller than the values observed for $KCu_2(H_3O_2)(SO_4)_2$, 0.55 Å,[4] and for $NaCo_2(D_3O_2)(MoO_4)_2$, 0.50 Å,[8] in relation with the chemical content with biggest ions in the present case. **FeH**, **FeD**, **CoH**, and **CoD** are isostructural to the manganese compounds, and their structures do not show any phase transitions with temperature down to 1.6 K.

Magnetic Properties. The temperature dependence of the magnetic susceptibility χ of **MnH** in an applied field of 100 Oe is shown in Figure 4. χ increases gradually from 300 to 32 K where a sudden jump takes place, followed by a rounded plateau down to 8 K where a final small decrease is observed. In the paramagnetic region, χ follows a Curie−Weiss law, $\chi = C/(T - \theta)$, with C = 8.94(2) emu K/mol and θ = −52.6 K. The effective moment $(8C)^{1/2}$ of 5.98 μ_B is close to the expected value of 5.92 μ_B. From the Curie constant C of 4.47 emu K per Mn and with S = 5/2, we deduced a value of the Landé factor g = 2.02, in good agreement with a ^{6}A ground state ion.[15] The alternating current (ac) susceptibilities reveal the presence of two peaks for the real component at 32.3 and 8.2 K and only one for the imaginary component at 32.3 K (Figure 4). It suggests that the sample contains a ferromagnetic phase that is responsible for the peaks at 32.3 K and another phase with an AF transition at 8.2 K. The isothermal magnetization at 4 K (Figure 5) shows a linear evolution between −50 and +50 kOe, with a very small discontinuity at low applied fields. All the results, including the neutron diffraction (see later), lead us to consider that the ferromagnetic phase is an impurity present at a very small level. Therefore, one would consider that **MnH** orders AF at 8.2 K.

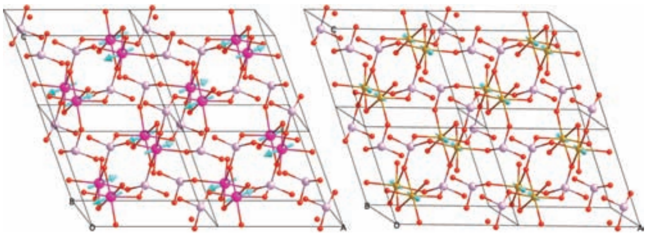

Figure 8. Orientations of the moments for **MnD** (left) and **FeD** (right) in the magnetic cell 2*a* × *b* × 2*c*.

For a sample of **FeH** with the black particles removed under a microscope the direct current (dc) susceptibility is weakly independent of temperature and displays a sharp peak at 11 K. The estimated susceptibility at 300 K is 25 times that expected for two Fe^{II} (S = 2) per formula unit (Supporting Information, Figure S10). The ac-susceptibility shows a peak at 11 K and a broad background with a maximum near 40 K. Following the neutron diffraction experiments, we concluded that the sharp peak at 11 K is due to the antiferromagnetic ordering of **FeH** and the high dc-magnetization is due to the magnetic large particles of iron oxides while the broad maximum in the low temperature region may be associated with the presence of nanoparticles of less than 20 nm. We note that the presence of magnetic iron oxides is common when working with iron in alkaline medium at high temperatures.

For **CoH**, in the paramagnetic region the susceptibility follows a Curie−Weiss law with C = 7.97(1) emu K/mol and θ = −17.1(3) K. χ increases gradually from room temperature and then strongly at around 10 K (Supporting Information, Figure S11). The ac-susceptibilities reveal the presence of a peak in both the real and the imaginary components at 12 K. The isothermal magnetization shows a very small hysteresis overlapping a Brillouin behavior saturating to 3.8 μ_B in 50 kOe (Supporting Information, Figure S7). The absence of any magnetic diffraction to the lowest temperature of 1.6 K (Figure 6) suggests that this compound does not order magnetically. The coincidental ferromagnetic ordering at 12 K for $Co_2(OH)_2MoO_4$; T_C = 12 K, C = 7.02(1) emu K/mol, Θ = +3.2(2) K, coercive field = 1400 Oe and remanant magnetization = 2 μ_B at 2 K (Supporting Information, Figure S12). Furthermore, the identification of two of its nuclear Bragg peaks in the diffraction patterns therefore confirms the latter is responsible for the anomaly.

Magnetic Structure Determinations. Figure 6 shows the neutron powder diffraction patterns recorded at low temperature (1.6 K) and above T_N for **Mn-D**, **Fe-D**, and **Co-D** as well as the difference. First of all, it clearly appears that for **Co-D**, both patterns

Table 6. Summary of the Magnetic Structure Refinement of MnD from Data Recorded at 1.6 K

				LRO			SRO	LRO+SRO
atom	x/a	y/b	z/c	M_x (μ_B)	M_z (μ_B)	M (μ_B)	M_x (μ_B)	M (μ_B)
Mn11	0. 125	0.25	0.125	3.90(3)	1.37(9)	3.61(3)	3.47(7)	5.01
Mn12	0. 125	0.75	0.125	−3.90(3)	−1.37(9)	3.61(3)	−3.47(7)	5.01
Mn13	0.375	0.25	0.375	−3.90(3)	−1.37(9)	3.61(3)	−3.47(7)	5.01
Mn14	0.375	0.75	0.375	3.90(3)	1.37(9)	3.61(3)	3.47(7)	5.01
Mn21	0.625	0.25	0.125	−3.90(3)	−1.37(9)	3.61(3)	−3.47(7)	5.01
Mn22	0.625	0.75	0.125	3.90(3)	1.37(9)	3.61(3)	3.47(7)	5.01
Mn23	0.875	0.25	0.375	3.90(3)	1.37(9)	3.61(3)	3.47(7)	5.01
Mn24	0.875	0.75	0.375	−3.90(3)	−1.37(9)	3.61(3)	−3.47(7)	5.01
Mn31	0.125	0.25	0.625	−3.90(3)	−1.37(9)	3.61(3)	−3.47(7)	5.01
Mn32	0.125	0.75	0.625	3.90(3)	1.37(9)	3.61(3)	3.47(7)	5.01
Mn33	0.375	0.25	0.875	3.90(3)	1.37(9)	3.61(3)	3.47(7)	5.01
Mn34	0.375	0.75	0.875	−3.90(3)	−1.37(9)	3.61(3)	−3.47(7)	5.01
Mn41	0.625	0.25	0.625	3.90(3)	1.37(9)	3.61(3)	3.47(7)	5.01
Mn42	0.625	0.75	0.625	−3.90(3)	−1.37(9)	3.61(3)	−3.47(7)	5.01
Mn43	0.875	0.25	0.875	−3.90(3)	−1.37(9)	3.61(3)	−3.47(7)	5.01
Mn44	0.875	0.75	0.875	3.90(3)	1.37(9)	3.61(3)	3.47(7)	5.01

Table 7. Summary of the Magnetic Structure Refinement of FeD from Data Recorded at 1.6 K

atom	x/a	y/b	z/c	M_y (μ_B)
Fe11	0. 125	0.25	0.125	3.55(3)
Fe12	0. 125	0.75	0.125	−3.55(3)
Fe13	0.375	0.25	0.375	−3.55(3)
Fe14	0.375	0.75	0.375	3.55(3)
Fe21	0.625	0.25	0.125	−3.55(3)
Fe22	0.625	0.75	0.125	3.55(3)
Fe23	0.875	0.25	0.375	3.55(3)
Fe24	0.875	0.75	0.375	−3.55(3)
Fe31	0.125	0.25	0.625	−3.55(3)
Fe32	0.125	0.75	0.625	3.55(3)
Fe33	0.375	0.25	0.875	3.55(3)
Fe34	0.375	0.75	0.875	−3.55(3)
Fe41	0.625	0.25	0.625	3.55(3)
Fe42	0.625	0.75	0.625	−3.55(3)
Fe43	0.875	0.25	0.875	−3.55(3)
Fe44	0.875	0.75	0.875	3.55(3)

are identical with a flat difference. Therefore, it can be definitely concluded that this compound does not order magnetically.

For **Mn-D** and **Fe-D**, numerous new Bragg reflections appear at low temperature in favor of antiferromagnetic ordering. These lines disappear at 7.8 and 11 K for **Mn-D** and **Fe-D**; temperatures defining T_N that agrees with the values deduced from magnetic measurements. For **Mn-D**, no further evolution of the neutron powder pattern is detected between 7.8 and 29 K. Therefore, it can be concluded that the ferromagnetic phase with a Curie temperature of 32 K is present at a very low level that is not detectable by diffraction techniques. In addition, the background exhibits broad humps characteristics of a short-range order (SRO) at all temperatures, the effect being more pronounced for **Mn-D**.[16]

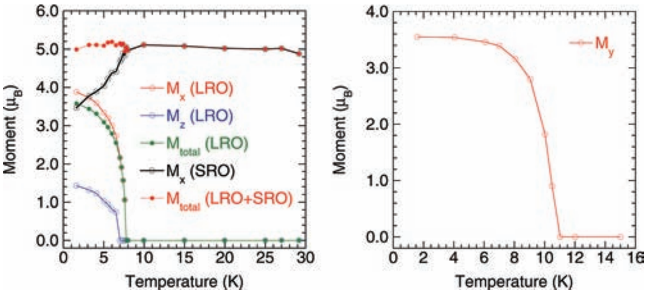

Figure 9. Temperature dependence of the active components of the magnetic moments for **MnD** (left) and **FeD** (right).

Since the magnetic Bragg reflections (Table 4) are not indexed using the nuclear cell parameters, the propagation vector cannot be (0, 0, 0), and we find that all magnetic lines can be indexed using a unit cell with $a_m = 2a_n$, $b_m = b_n$ and $c_m = 2c_n$ (m for magnetic and n for nuclear), that is, a $k = (^1/_2, 0, ^1/_2)$ propagation vector. To study the magnetic structure, we determined the associated magnetic structure with the help of Bertaut's representation analysis method,[17] applied to $I2/m$ space group. Two one-dimensional irreducible representations (IR), Γ_1 and Γ_3 (Table 5) are associated to basis vectors (magnetic structures).[18]

The two models in Table 5 differ by the orientation of the magnetic moments, either in the *ac* plane (Γ_1) or along the *b* axis (Γ_3). The other components (M_y for Γ_1 and M_x and M_z for Γ_3) must be zero otherwise a ferromagnetic contribution would appear. Both models result in antiferromagnetic order inside the MO_6 infinite chains running along the *b* axis. To solve the structure, we have to find the relative distributions inside the $2a \times b \times 2c$ unit cell with AF chains. We therefore proceed by trial and error to test the various possibilities. The best fits between the observed and the calculated diffraction patterns are shown in Figure 7. Finally, a similar model applies for both compounds but according to Γ_1 for **MnD** and to Γ_3 for **FeD**. Figure 8 shows the corresponding magnetic structures.

To take into account the presence of the SRO magnetic structure, a second magnetic phase has been introduced in the refinement using the same model as the long-range order (LRO) structure. For **MnD**, the M_z component of the SRO structure was not significant. However, the refinement does not converge for **FeD**, probably in relation with the weakness of the signals. Tables 6 and 7 summarize the refinement results.

The thermal evolution of the magnetic structures has been followed by refinement of data recorded at various temperatures. From the corresponding evolution (Supporting Information, Table S4, Figure 9) for **MnD**, it appears that between 1.6 and 6.5 K, the resulting LRO moment progressively turns toward the *a*-axis. Between 7 and 7.6 K, the M_z component becomes non significant and the moments lie along the *a*-axis. On the other hand the SRO magnetic component increases up to T_N, then remains nearly constant. A reverse evolution is evidenced for the coherence length that decreases above T_N after a plateau at lower temperatures. However, the most surprising result concerns the similar contributions of the LRO and SRO structures to the overall Mn magnetic moments that remain close to the expected 5 μ_B, the biggest deviation being lower than 4%. At 1.6 K, both contributions are nearly equal, but with increasing temperature the SRO contribution becomes dominant. This means that within the considered temperature range, complete 3D ordering is not achieved in the whole sample. However, the model does not allow one to get a better description of the SRO structure: localized domains or oriented domains or another model. A measurement at room temperature reveals that SRO is no more evidenced. For **Fe-D**, the temperature dependence of the magnetic moment is simpler since it is oriented along the *b*-axis of the unit cell (Supporting Information, Table S5 and Figure 9).

■ CONCLUSION

The nuclear and magnetic structures of three examples, $KM^{II}_2(D_3O_2)(MoO_4)_2$ where M = Mn, Fe, or Co, of a structural variant of natrochalcite (*I*2/*m* space group) have been determined which involved the rotation of the *a*- and *c*- axes about the *b*-axis compared to those having the *C*2/*m* space group. Interestingly, the nuclear structures remain the same with edge-sharing chains of octahedra bridged by D_3O_2 and MoO_4. While the cobalt compound do not exhibit magnetic ordering, in contrast to its sodium analogue, the manganese and iron compounds display both short-range and long-range orderings below 8 and 11 K, respectively. The magnetic structures of the latter two expand over four nuclear cells with a propagation vector $k = {}^{1}/_{2}, 0, {}^{1}/_{2}$. The moments are antiparallel within the chains but are perpendicular (M = Mn) and parallel (M = Fe) to the *b*-axis. The overall resultant moment is zero.

■ ASSOCIATED CONTENT

Ⓢ **Supporting Information.** Further details are given in Figures S1−S12 and Table S1−S5. This material is available free of charge via the Internet at http://pubs.acs.org.

■ AUTHOR INFORMATION

Corresponding Author

*E-mail: vilminot@ipcms.u-strasbg.fr (S.V.), kurmoo@unistra.fr (M.K.). Phone: 00 33 3 88 10 71 28 (S.V.), 00 33 3 68 85 12 31 (M.K.).

■ ACKNOWLEDGMENT

This work was funded by the CNRS, Université de Strasbourg and CEA (France).

■ REFERENCES

(1) http://www.mindat.org/min-2853.html. (a) Palache, C. *Am. J. Sci.* **1939**, *237*, 451.(b) Palache, C.; Berman, H.; Frondel, C. *The System of Mineralogy of James Dwight Dana and Edward Salisbury Dana*, Yale University, 7th ed.; John Wiley and Sons, Inc.: New York, 1951; Vol. II, p1837.

(2) (a) Cord, P.-P.; Courtine, P.; Pannetier, G. *C. R. Acad. Sci. Paris, Serie C* **1970**, *270*, 946. (b) Clearfield, A.; Sims, M. 1.; Gopal, R. *Inorg. Chem.* **1976**, *15*, 335. (c) Pezerat, H. *Bull. Soc. Fr. Mineral. Cristallogr.* **1967**, *90*, 549. (d) Tardy, M.; Bregeault, J.-M. *Bull. Soc. Chim. France* **1974**, 1866. (e) Rumanova, I. M.; Volodina, G. F. *Doklady Acad. Nauk SSSR* **1958**, *123*, 78 (in Russian).

(3) (a) Giester, G. *Z. Kristallogr.* **1989**, *187*, 239. (b) Giester, G.; Zemann, J. *Z. Kristallogr.* **1987**, *179*, 431.

(4) (a) Chevrier, G.; Giester, G.; Jarosch, D.; Zemann, J. *Acta Crystallogr.* **1990**, *C46*, 175. (b) Chevrier, G.; Giester, G.; Zemann, J. *Z. Kristallogr.* **1993**, *206*, 7. (c) Krickl, R.; Wildner, M. *Eur. J. Mineral.* **2009**, *21*, 65. (d) Krickl, R.; Wildner, M. *Eur. J. Mineral.* **2007**, *19*, 805.

(5) Cornell, R. M.; Schwertmann, U. *The Iron Oxides, Structure, Properties, Reactions, Occurrence and Uses*; VCH Publishers: Weinheim, Germany, 1996.

(6) Vilminot, S.; André, G.; Bourée-Vigneron, F.; Richard-Plouet, M.; Kurmoo, M. *Inorg. Chem.* **2007**, *46*, 10079.

(7) Vilminot, S.; André, G.; Richard-Plouet, M.; Bourée-Vigneron, F.; Kurmoo, M. *Inorg. Chem.* **2006**, *45*, 10938.

(8) Vilminot, S.; André, G.; Bourée-Vigneron, F.; Baker, P. J.; Blundell, S. J.; Kurmoo, M. *J. Am. Chem. Soc.* **2008**, *130*, 13490.

(9) Rodriguez-Carvajal, J. *FULLPROF: Rietveld, Profile Matching and Integrated Intensity Refinement of X-Ray and/or Neutron Data*, Version 3.5d; Leon-Brillouin Laboratory: CEA Saclay, Gif sur Yvette Cedex, France, 2005.

(10) Boultif, A.; Louer, D. *J. Appl. Crystallogr.* **2004**, *37*, 724.

(11) (a) Shannon, R. D.; Prewitt, C. T. *Acta Crystallogr.* **1969**, *B25*, 925. (b) Shannon, R. D.; Prewitt, C. T. *Acta Crystallogr.* **1970**, *B26*, 1046.

(12) Nakamoto, K. *Infrared and Raman Spectra of Inorganic and Coordination Compounds*, 5th ed.; John Wiley & Sons: New York, 1997.

(13) Beran, A.; Giester, G.; Libowitzky, E. *Mineral. Petrol.* **1997**, *61*, 223.

(14) Sheldrick, G. M. *SHELX97-2*; University of Göttingen: Göttingen, Germany, 1997.

(15) Herpin, A. *Theorie du Magnétisme*; Presses Universitaire de France: Paris, 1968.

(16) (a) Ben Salah, M.; Vilminot, S.; André, G.; Bourée-Vigneron, F.; Richard-Plouet, M.; Mhiri, T.; Kurmoo, M. *Chem. Mater.* **2005**, *17*, 2612. (b) Ben Salah, M.; Vilminot, S.; André, G.; Richard-Plouet, M.; Bourée-Vigneron, F.; Mhiri, T.; Kurmoo, M. *Chem.—Eur. J.* **2004**, *10*, 2048.

(17) Bertaut, E. F. *Acta Crystallogr., Sect. A* **1968**, *24*, 217.

(18) *KAREP*, a program for calculating irreducible space group representations; Hovestreydt, E.; Aroyo, I.; Sattler, S.; Wondratschek, H. *J. Appl. Crystallogr.* **1992**, *25*, 544.Rodriguez-Carvajal, J. *BASIREPS, a program for calculating non-normalized basis functions of the irreducible representations of the little group Gk for atom properties in a crystal*; Laboratoire Léon Brillouin (CEA(CNRS): CEA Saclay, Gif sur Yvette Cedex, France, 2004.